On the mechanism for edge localized mode mitigation by supersonic molecular beam injection

T. Rhee,[1,a)] J. M. Kwon,[1] P. H. Diamond,[1,2] and W. W. Xiao[1,3]
[1]WCI Center for Fusion Theory, National Fusion Research Institute, Daejeon 305-333, Korea
[2]CMTFO and CASS, UCSD, San Diego, California 92093 USA
[3]Southwestern Institute of Physics, P.O. Box 432, Chengdu, China

We construct a diffusive, bi-stable cellular automata model to elucidate the physical mechanisms underlying observed edge localized mode (ELM) mitigation by supersonic molecular beam injection (SMBI). The extended cellular automata model reproduces key qualitative features of ELM mitigation experiments, most significantly the increase in frequency of grain ejection events (ELMs), and the decrease in the number of grains ejected by these transport events. The basic mechanism of mitigation is the triggering of small scale pedestal avalanches by additional grain injection directly into the H-mode pedestal. The small scale avalanches prevent the gradient from building-up to marginality throughout the pedestal, thus avoiding large scale transport events which span the full extent of that region. We explore different grain injection parameters to find an optimal SMBI scenario. We show that shallow SMBI deposition is sufficient for ELM mitigation. © 2012 American Institute of Physics. [doi:10.1063/1.3685720]

I. INTRODUCTION

H-mode is an improved tokamak confinement state in which turbulent energy, momentum, and particle transport are all reduced simultaneously.[1] Due to its robustness and potential for steady state operation, H-mode is considered to be a prime candidate among the possible operation modes for next generation machines, such as International Thermonuclear Experimental Reactor (ITER). The distinguishing features of H-mode plasmas include pedestal formation (i.e., edge transport barrier) and ELMs, related to pedestal instability. In the pedestal, turbulent transport is suppressed, most likely by strong $E \times B$ shear flows. The resulting steep equilibrium gradients in the pedestal provide a boundary condition for the core plasma which strongly influences the overall plasma performance. In the state of suppressed micro-turbulence and anomalous transport, ELMs induce large episodic releases of stored energy and particles from the pedestal.

The understanding and control of ELMs are critical to the improvement of fusion performance in future machines. The ELM has two effects on steady state tokamak operation. The global confinement degradation and transient heat loads on plasma facing components (PFCs) caused by ELMs raise serious challenges to steady state operation, especially considering the substantially higher stored energy of future tokamak plasmas.[2] On the other hand, ELMs are also expected to play a beneficial role by eliminating fusion ash and impurities which induce unfavorable effects. These issues motivate the extensive ongoing experimental studies of ELM control. Experiments on ELM control using active external actuators are classified as mitigation or suppression. The former refers to when a external actuator reduces ELM heat loads on the PFC. Pellet injection demonstrates that paced pellet injection triggers ELMs.[3] Using this technique, sequential pellet injection at frequencies higher than ELM frequency reduces the peak heat load on the PFC.[4,5] Suppression is when a external actuator strongly inhibits or eliminates ELMs in the pedestal. Ergodization of the magnetic field, after a first attempt,[6] results in ELM suppression.[7,8] On the other hand, the theoretical understanding of mitigation/suppression processes is still in its infancy, since the complexity of applying these methods to large, steady state devices such as ITER leaves many questions open.

Recent experiments on HL-2 A demonstrated that SMBI (which is a fuel injection method[9]) into the H-mode pedestal can mitigate ELMs significantly.[10] A summary of the principal experimental results is

(i) The most effective location for neutral deposition is just inside the separatrix.
(ii) After SMBI, the ELM frequency increases 2–3.5 times and the H_α signal, which represents the amplitude of ejection, decreases by $\sim 1/3$.
(iii) Mitigation is sustained for the duration of the influence time τ_I, which is $\sim \tau_{ELM}$ for the case shown in Fig. 4 of Xiao et al.,[10] where τ_{ELM} is ELM period. After τ_I, the ELM behavior resumes its pre-SMBI characteristics.
(iv) Experiments varying the SMBI pulse duration indicate that too weak or too short an SMBI pulse does not produce ELM mitigation.
(v) Global energy confinement is not much affected, though the pedestal density profile broadens slightly.

Subsequent experiments on KSTAR have also demonstrated ELM mitigation by SMBI injection.[11] Experiments on KSTAR have shown mitigated ELMs during several hundreds of *ms*—much longer than that of HL-2 A experiments.

a)Electronic mail: trhee@nfri.re.kr.

All these results concerning ELM mitigation by SMBI suggest a promising alternative approach to ELM control.

Despite the importance and urgency of the issues, the physics of ELM related phenomena, and especially mitigation, remains poorly understood. This is largely due the great complexity of the problem. Also, a first principles simulation of ELM mitigation is still beyond the scope of the most advanced present day simulation codes. Thus, it is an interesting idea to consider whether we can address and understand the key features of the SMBI ELM mitigation experiments using a very simple model. Probably, the simplest model for describing episodic (i.e., bursty) transport phenomena in H-mode plasmas is the cellular automata (CA) model, based on the bi-stable automata rule.[12] The CA model successfully explained complex phenomena related to various aspects of turbulent transport in tokamak plasmas, e.g., avalanching, long time correlations,[13] flux probability distribution and spectra, self similarity,[14] transport scaling and the effect of $E \times B$ shear,[15,16] and the importance of boundaries and edge turbulence.[17,18] Also, it was shown that the CA model can capture the key features of internal and edge transport barrier formation.[12,19,20] In this paper, we investigate ELM mitigation by SMBI using a CA model. When we consider the enormous difficulties involved in more detailed modeling of the SMBI-induced mitigation phenomena, the virtues of the simplest model are apparent: it is a good test of the robustness of the mechanisms, i.e., it can explain the key features of mitigation by retaining only the most essential elements of H-mode pedestal dynamics. It can also provide useful insight with which to guide experiments, by providing a guide to optimized SMBI operation parameters. Also, it could help guide future, "first principle," simulation development.

The remainder of this paper is organized as follows. In Sec. II, we introduce the simulation model. The detailed rules of the bi-stable cellular automation (with a hard gradient boundary) are described here. In Sec. III, we investigate the mechanism of ELM mitigation by SMBI. In that section, we present detailed analysis of mitigation and explore the effects of SMBI parameter changes to find an optimal SMBI scenario. Finally, the conclusions are presented in Sec. IV.

II. MINIMAL MODEL FOR ELM MITIGATION

The minimal constituents to reproduce ELMy H-mode in a CA model[20,21] are (i) transport by gradient driven micro-turbulence, (ii) neoclassical transport, dominant when turbulence is quenched, (iii) $E \times B$ shear flow suppression of turbulent transport, as in a transport barriers, (iv) a "hard" gradient limit and resulting large transport as by MHD instabilities associated with ELMs. The model CA rules are constructed to capture the key features of these constituents.

First, "flips" in the CA model represent transport by micro-turbulence. The turbulent transport is driven by micro-instabilities drawing free energy stored in temperature or density gradients.[22] This process controls the range of the temperature gradient from the linear threshold gradient to the H-mode transition[23] and leads to a strong thermal flux as shown in Fig. 1. That describes the turbulent heat flux change set by the increase of temperature gradient and thus shows the turbulent heat flux change during the L-H transition.[24] The transport in those cells in the unstable gradient regime is given by the so called the "flipping" rule, i.e., a fixed number of grains Γ_F are moved in the downhill direction if the local threshold is exceeded. Cells become unstable if the slopes are in the range $Z_{C1} < Z_i < Z_{C2}$, where Z_i is determined by neighboring cells, $Z_i = H_i - H_{i+1}$, and H_i is the number of grains in a i cell.

Second, the neoclassical transport is represented by constant, ambient diffusion in the CA. The neoclassical transport is associated with collisions in plasma. Thus, this phenomenon is the fundamental "irreducible" transport, always present, though its strength is much smaller than that of transport by micro-turbulence. The S-curve in Fig. 1 shows the neoclassical transport dominates in the steep temperature gradient region, i.e., in the H-mode. The neoclassical transport in the CA model is given by $\Gamma_D = D_0(Z_{i-1} - Z_i)$. Here, D_0 is a diffusion coefficient. Although the transport by the diffusion is smaller than that due to toppling, the small diffusion erases the inhomogeneities generated by baseline random fueling and changes the dynamics of toppling induced transport from a self-similar structure with a continuous spectrum to a quasi-periodic event with a size spanning nearly the full pedestal width[27] Clearly, the later is more similar to ELM phenomena.

Third, the suppression of turbulent transport is expressed as a window of CA stability, i.e., the absence of a flipping state. The physics which underlies this CA stability window is $E \times B$ shear suppression. The turbulent transport is suppressed by $E \times B$ sheared flow decorrelation of turbulence. Sheared flow is, in turn, determined by the gradient of the pressure gradient as

$$V'_E \simeq \frac{c}{eB}\left(\frac{\nabla p}{n}\right)',$$

where n is plasma density, c is speed of light, and e is unit charge. On the S-curve in Fig. 1, the transport reduction is shown as the shallower slope in the large temperature gradient range (H-mode region). Transport suppression is modeled as steep gradient stability in the CA. For the slopes $Z_{C2} < Z_i < Z_{C3}$, flipping and toppling (described following paragraph) are suppressed, but the ambient diffusion continues to operate. Note that the stability window representation is plausible since the flow is itself driven by local ∇p, via
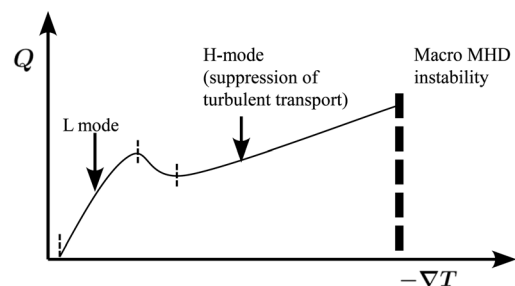

FIG. 1. S curve analogy of automata rules. Dashed bold line means the hard limit and dashed lines are critical slope for the unstable range.

radial force balance. Also observe that the stability window is necessary in order to obtain identifiable L-mode and H-mode profile states.

Fourth, transport by MHD instabilities is modeled by a hard threshold for toppling in the CA model. The MHD instabilities in the pedestal are thought to be related to ELMs in the H-mode plasma. The ELMs are of three principal types, types I (giant ELMs), II (grassy ELMs), III (small ELMs), and unnamed types. The ELM processes are illustrated by the simple Fig. 2, though the dynamics of ELMs is not yet fully understood.[25] The pressure profile instability criterion for each mode is determined by the combination of bootstrap current and pressure gradient. However, in the H-mode pedestal, the bootstrap current is directly proportional to the pressure gradient

$$j_{bs} \sim \frac{dp}{dr} \frac{1}{B_p},$$

where j_{bs} is bootstrap current, B_p is poloidal B field, and p is pressure.[26] Thus, the pedestal pressure gradient is the fundamental physical quantity which determines ELM stability. ∇p-driven ELMs have the common feature of setting a hard upper limit on the achievable pressure gradient. The particle and heat transport by ELMs restore the plasma to an MHD stable state. In the CA model, we model this hard upper pressure gradient limit feature as an upper limit on the pile slope Z_{C3}. If the slope hits the hard limit, then all "locally" excess grains are forced to topple, according to the rule: $\Gamma_T = 1 + (Z_i - Z_{C1})/2$.

The remainder of the model, needed to compose a complete CA model, is the rules for evolving the CA system. The model system is composed of cells, each of which is analogous to an eddy. The cell size may thus be thought of as a local turbulence correlation length. The grains in ith cell, H_i, are evolved in discrete time steps. Each step has two stages of evolution: deposition and transport. During the first stage, grains are deposited according to the fueling/heating rule and N_d grains are randomly scattered on the system. In the second stage, the cells are examined to determine whether they satisfy the local transport criterion. A closed boundary condition is employed for the left $i = 1$. An open boundary condition is applied at the right boundary cell $i = L$, where L denotes the system size. For this boundary

TABLE I. Analogy between transport model and cellular automata model.

Turbulent transport in toroidal plasma	Cellular automata model
Localized fluctuation(eddy)	Grid site(cell)
Local transport mechanism:	*Automata rules:*
Critical gradient range for micro-turbulence	Unstable slope range
Moderate local eddy-induced transport	Flipping of fixed number of grains
Flow shear suppression of turbulence	Steep slope stable range
Critical gradient for MHD even	Hard limit
Strong MHD-induced transport	Large toppling of grains
Total energy/particle content	Total number of grains (total mass)
Heating noise/background fluctuations	Random input of grains
Energy/particle flux	Grain flux
Mean temperature/density profiles	Average slope of system
Transport event	Avalanche

condition, the net grain flux is always out going and $Z_L = H_L$. We summarize the analogy between transport in the toroidal plasma and the CA model in Table I.

We add the SMBI to the CA simulation to test ELM mitigation. The main role of SMBI in plasmas is to provide edge fueling with a variable range of penetration. We model this by additional grain injection (AGI) with a spatially variable shape and deposition rate. Figure 3 shows the parameters defining the AGI pulse shape. τ_{dep} defines the time duration of AGI pulse, which is set in accord with the SMBI induced H_α signal in the experiments.[10] This pulse injection is repeated with time separation τ_{rep}. We choose the most simple form for the spatial deposition distribution, i.e., all grains are deposited at a single cell. δ_n is a fixed number of AGI grains per step, corresponding to the strength of SMBI.

We choose a set of CA parameters for ELMy H-mode. The values of the parameters are: $Z_{C1} = 8, Z_{C2} = 20$, and $Z_{C3} = 30$ for instability threshold; $D_0 = 0.08$ for the diffusion coefficient; $N_d = 10$ for the baseline grain deposition. Increasing N_d reduces the ELM period, reflecting a balance between fueling and transport. Z_{C3} variation affects the confinement time and the ELM period. An increase of the Z_{C3} value increases the pedestal slope, so that the total number of grains in the system increases and the confinement time also increases. An increase of the hard limit gradient also raises the number of grains toppled. To balance fueling and increased transport by a ELM event, the inter-ELM period also increases. The total number of time steps are 3×10^5. We choose the time window from the time step 1×10^5 to 3×10^5 to ensure stationarity of statistics of the averaged simulation data during long time steps. Various AGI parameters are explored for the study of ELM mitigation in Sec. III.
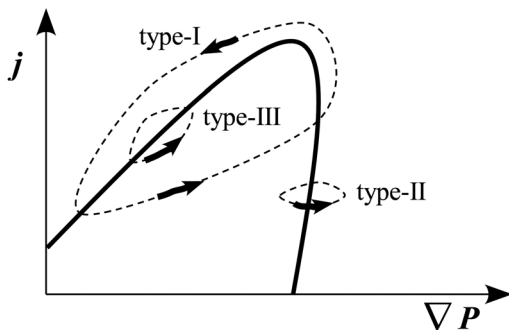

FIG. 2. Figure explaining ELM trajectory of types I, II, and III in the pressure gradient ∇P and current density j. Inner area of black thick line is stable region from peeling-ballooning instabilities. Dashed lines and arrows indicate possible trajectory of indicated ELM type.
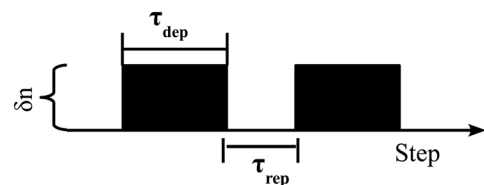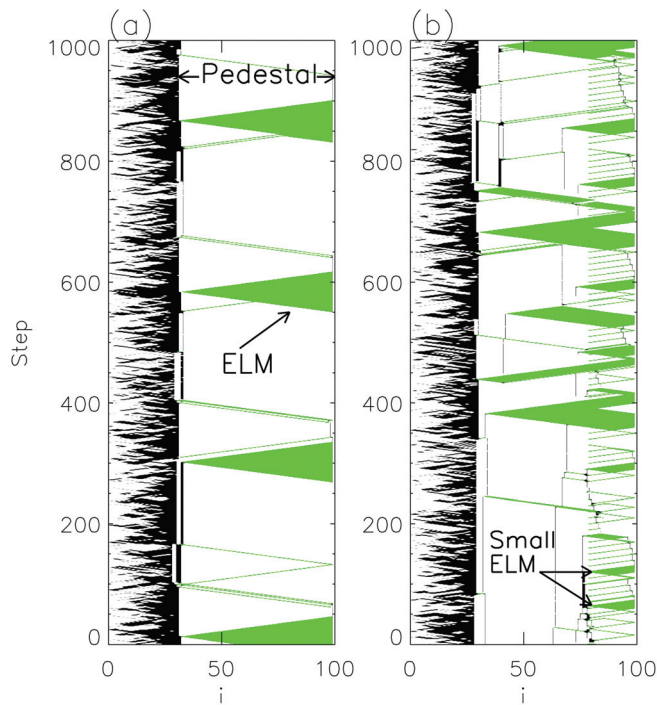

FIG. 3. AGI pulse timing diagram.

FIG. 4. (Color) Space time pattern of the pile (a) without injection and (b) with injection: white cells are stable, black cells are unstable, and green cells are hard limit unstable. Large size ELMs without injection become smaller, more frequent ELMs.

III. ELM MITIGATION IN THE CELLULAR AUTOMATA MODEL

A. Basic mechanism of the ELM mitigation

We investigate the dynamics of large scale toppling events occurring in the H-mode CA without AGI. Figure 4(a) shows the spatio-temporal pattern of CA evolution. In the core region ($1 < i < 30$), the CA transport events are produced by the flipping events, indicated by the black color. Outside of this region, where the CA starts to form a steep gradient, the transport is mainly driven by toppling events induced by the hard limit, i.e., grain transport caused by hitting the hard boundary limit, which imposes the local profile stability criterion. The green colored cells show these avalanche events. They have a triangular spatio-temporal structure. Otherwise, the cells indicated by white color are steep gradient stable, i.e., reflecting turbulent transport suppression by equilibrium $E \times B$ flows, as occurs in the pedestal.

These large green triangular events have many common features with the ELMs observed in H-mode plasmas. As seen in Fig. 4(a), they span the whole pedestal region and cause a global collapse of the pedestal pressure. Toppling avalanches start at the pedestal edge cell. The toppling event starts due to void formation and cascades inward from the boundary,[28] then triggering a discharge of the entire pedestal, as shown in Fig. 5(a). The void formation and inward propagation cascade linked to two neighboring cells: the inner cell exceeds the hard limit while the outer cell is stable. This cascade leaves the cells at the upper hard limit unstable after passing, thus causes the full pedestal region to ultimately collapse. The inward void cascade, triggered at the pedestal edge, appears to give rise to avalanches of the size comparable to the pedestal
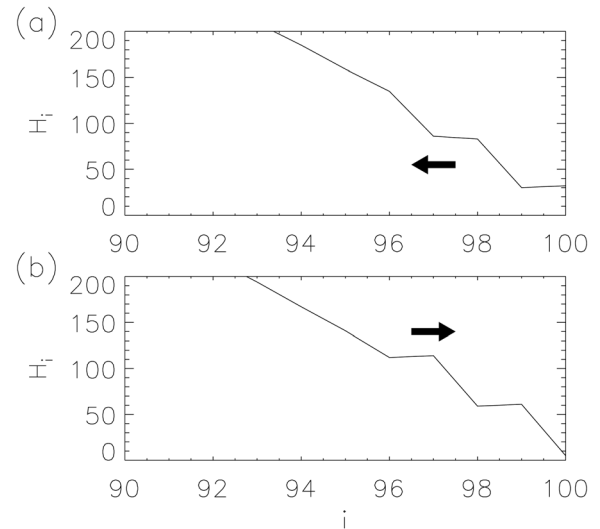

FIG. 5. Formation of two different toppling cascade types, (a) void and (b) clump type. Arrow shows the propagation direction of toppling cascade.

width. The correlation in length of such collective motion can be regarded as a signature of self organized criticality (SOC) due to simple toppling rules, as investigated by Hwa and Kadar.[29]

This void induced toppling cascade propagates up to the pedestal top. At the pedestal top, the toppling cascade is reflected backward (i.e., down the slope) because of the sharp gradient discontinuity (drop) at the boundary between the core and pedestal. Thus, the void does not enter the core region. The reflection changes the type of propagation from an ingoing void type to an outgoing clump type.[28] The clump type is composed of a stable cell and a neighboring cell occupied beyond the hard upper limit, as shown in Fig. 5(b). This cascade leaves the cells stable after passing and, thus, causes the termination of the toppling cascade. We see that combining basic, physically motivated toppling rules and a local hard gradient limit can yield ELM-like behaviour in a very simple model.

These quasi-periodic events occur in a relatively short time interval (~ 70 steps), which corresponds to $3 \times 10^{-3}\tau_p$, where τ_p denotes the grain confinement time of system. The calculated grain flux is ~ 500 times higher than the flux from the baseline diffusion, which mimics the neoclassical transport. The averaged time interval between the events is 200 steps, $\sim 9 \times 10^{-3}\tau_p$. Hereafter, we refer to these types of global (on the pedestal scale) avalanches in the CA as "ELMs."

When we apply AGI in the H-mode CA, the spatio-temporal pattern of the discharge dynamics changes drastically. Here, we use the simplest form of AGI to investigate the basic features of ELM mitigation. AGI is applied at every 10 time steps as a single pulse, with time duration of one step at $i = 80$, which is the pedestal base. The amount of additional grains per "one" injection is 20. Thus, the amount injected corresponds to a modest 2.6% of the average pedestal density n_0. As seen in Fig. 4(b), the green regions with toppling events show qualitatively different behavior. The quasi-periodic avalanches observed in the case without AGI are replaced by aperiodic transport events with irregular size
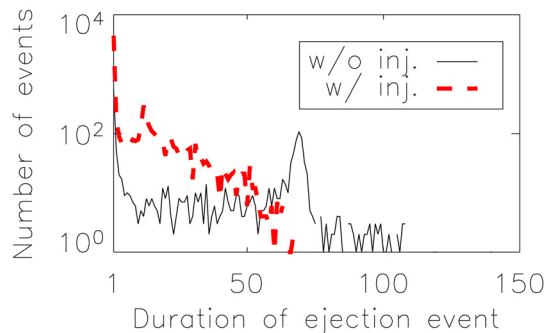
FIG. 6. (Color online) Avalanche size distribution of with (dashed line) and without (solid line) SMBI.

and shape. Also, we do not observe the continuous grain ejections caused by big avalanches, but instead more frequent and smaller grain ejections. These qualitative changes manifest the essential features of the observed ELM mitigation. We note that basic trends of the mitigated states described here persist for a wide range of AGI parameters. This point will be addressed in Sec. III B.

A study of avalanche size distribution shows the qualitative changes more clearly. In Fig. 6, we compare the avalanche size distribution for the case with and without AGI. Here, the size of an avalanche is defined as the continuous duration time of the grain ejection event at the pedestal edge. The solid curve for the case without AGI has a peak at size ~ 70, which corresponds to an average size of the original ELM. There are also big events with size ~ 100. It is notable that in this case, the strong isolated peak implies a regular or quasi-periodic ELM. Compared to the solid curve, the dashesd curve shows noticeable changes. The large isolated peak disappears, and the distribution takes a broader form, decreasing with event size, which implies more irregular dynamics dominated by smaller avalanches.

Figure 7 shows a zoom of the case with AGI. The case with AGI (i.e., the mitigated state) is characterized by (i) small size toppling events extending from the location of AGI to the pedestal edge and (ii) fragmented green triangles covering wider regions. Figure 7(a) shows the zoom of the
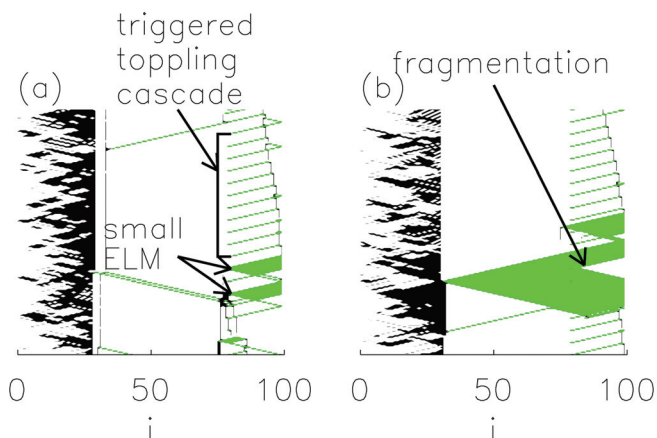
former small size events. These are triggered by AGI and pump grains out of the pedestal. This can be viewed as a process for controlled release of the pedestal pressure. The zoom of a fragmented green triangle in Fig. 7(b) shows that the cascade of toppling events (which originated in the core) stops at the injection location. There, a large grain ejection event fragments into smaller ones which ultimately cross the boundary.

This fragmentation process is straightforward to understand if we look at the changes of pedestal structure caused by AGI. In Fig. 8, averaged pedestal slopes are plotted for the case with and without AGI. The case without AGI shows a modest increase of the pedestal slope toward the edge. On the other hand, the case with AGI shows an abrupt decrease of the slope near the deposition location of AGI ($i = 80$ in this case). We can see that AGI induced pedestal pressure release is evident over the outer region of the injection location. To induce a global avalanche covering the whole pedestal, the profile gradients over the pedestal must be close to the hard limit, so as to ensure the cascade topples and extends from site to site. However, the case with AGI has much less steep local gradients outside of the injection location, so the cascade tends to stop after reaching the region of slope inhomogeneity. This mechanism causes the fragmentation of the large avalanches into smaller ones and results in the change in avalanche size distribution shown in Fig. 6. Smaller avalanches replace large avalanches, i.e., fewer large avalanches appear. We remark here that it would also be interesting to explore the impact of such sharp pedestal slope variation on peeling-ballooning mode eigenfunction structure and stability. Such consideration is potentially relevant to the effect of SMBI on Type-I ELMs

B. Effect of injection location and strength

We studied the effects of a change in injection location. Figure 9(a) shows the avalanche size distribution for various different injection locations. We find that the pedestal base ($i = 70$) and edge ($i = 100$) injection show effective ELM mitigation, i.e., disappearance of the large avalanche peaks and an increase in the number of smaller size events. However, if the injection location moves deeper toward the inside, AGI has little effect. The case with pedestal top injection ($i = 30$) shows a strong peak at the global avalanche size, as compared to the case without AGI. The case of

FIG. 7. (Color) Mitigated ELMs as shown in the space time pattern of (a) small ELMs and (b) fragments of a big ELM.
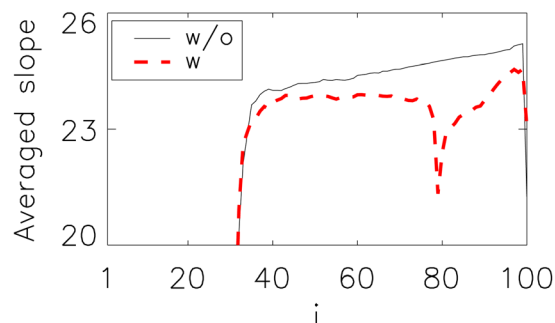

FIG. 8. (Color online) Averaged profile slope without (solid) and with (dashed) injection.
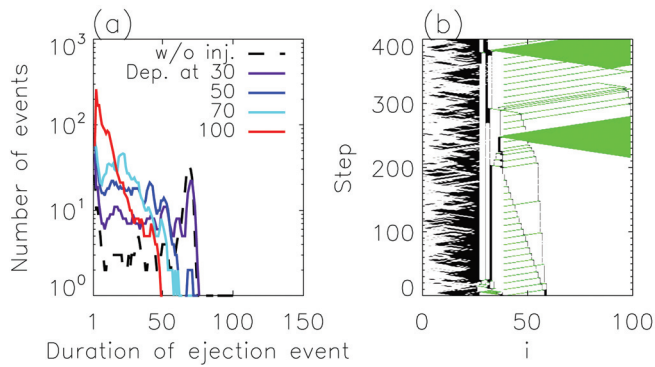
FIG. 9. (Color) (a) Avalanche size distribution for various injection locations and (b) space time pattern for pedestal top injection.

middle injection is mixed, i.e., global avalanches still appear, though the number of the events is reduced.

We can understand the decline of the mitigation effectiveness for deeper injection by inspecting the enlarged spatio-temporal window of the case with injection at the pedestal top. In Fig. 9(b), the AGI induced release of pedestal pressure—the toppling cascade indicated by green dotted lines—is not so effective as compared to the case of shallow injection (e.g., $i = 80$ case in Fig. 7(a)). Due to the long travel path of the cascade, avalanches often stop around the middle of the pedestal, implying an accumulation of grains in the middle, and a consequent limitation of the reduction in the pedestal pressure gradient. Because of this limitation, the profile tends to self-organize into a globally marginal state close to the hard limit. The fragmentation of big avalanches is, therefore, not efficient, and global avalanches reappear.

Spatially broader AGI deposition also shows ELM mitigation with sufficient injection strength. We tested the AGI with spatial injection width varying from 3 to 15 cells with the center at $i = 80$, for two different injection strengths of 11 and 21 grains. For the case of strong AGI as shown in Fig. 10(a), the avalanche size distributions show ELM mitigation for all cases. The average slopes in Fig. 10(b) manifest deformation of the slope for all cases. For the case of weak AGI strength, the avalanche size distributions in Fig. 10(c) indicates that broader AGI deposition is less effective for ELM mitigation. Consideration of the averaged slopes of the case with weak AGI strength shown in Fig. 10(d) suggests that the reduced effectiveness is caused by the consequent smaller deformation of the profile slope. The broader AGI with lower strength reduces the deposition strength at any given cell, so the resulting profile deformation weakens. We see that mitigation is not affected by detailed AGI parameters, if it generates sufficient gradient inhomogeneity. This suggests that SMBI may be effective in mitigating Type-I ELMs if it drives pedestal gradient inhomogeneities on a scale smaller than that of the peeling-ballooning eigenfunction.

We performed combined scans of the injection location and strength. In Fig. 11, the averaged ELM frequency and grain flux are plotted for different injection locations and strengths. The values are normalized by the case without AGI. The effect of ELM mitigation appears as an increase of frequency and a decrease in amplitude, as can be seen in Fig. 11. The trend of effective mitigation for shallow injection is also evident here. We found that for a given injection location, there is a minimum strength required to see mitigation effects. The minimum strength corresponds to the number of grains required to exceed the upper hard limit at a given
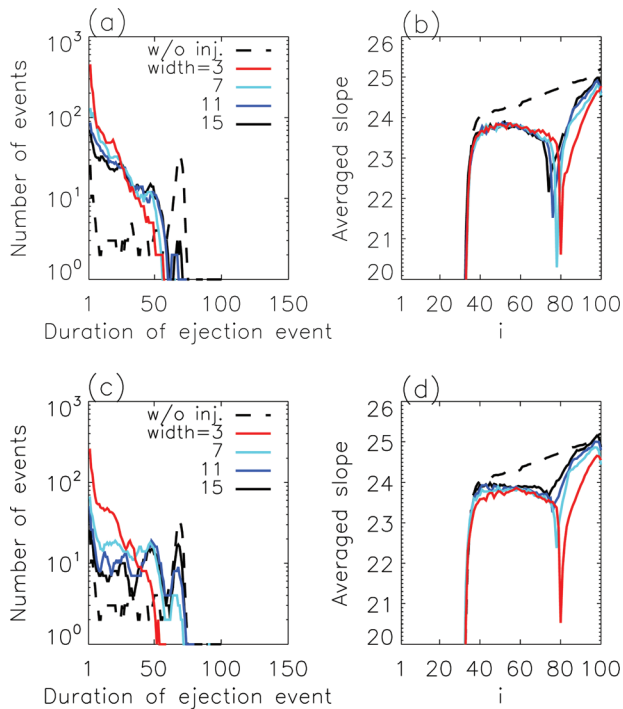

FIG. 10. (Color) Avalanche size distribution and averaged slope of two different injection strength: (a), (b) 21 grains and (c), (d) 11 grains. Colors indicate the spatial extent of injection with center at $i = 80$.
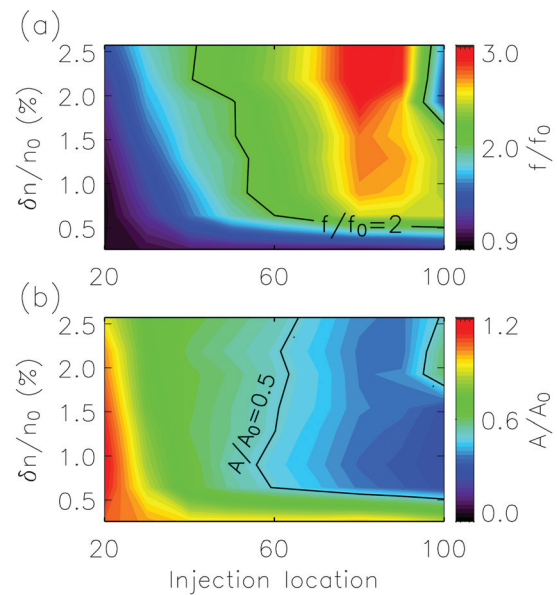

FIG. 11. (Color) Averaged (a) frequency and (b) amplitude of ELMs for various injection location and number of injection grains. Number of injected grains normalized by averaged pedestal density is shown by the vertical axis. Injection location is represented by the horizontal axis. The amplitude and frequency indicated by color contour are normalized by those values without AGI.
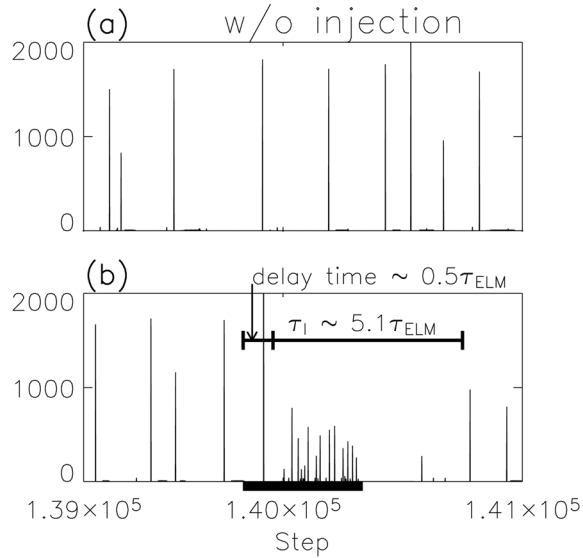
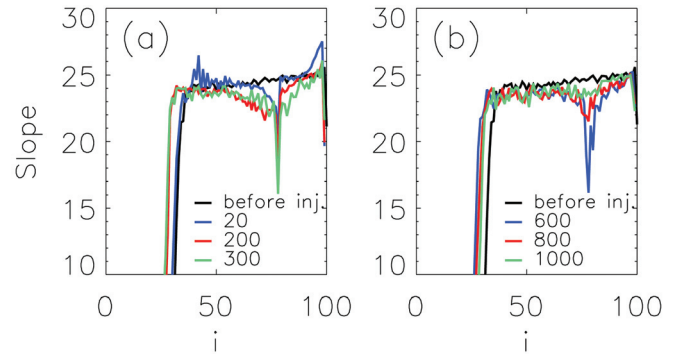FIG. 12. Edge flux (a) without and (b) with additional grain injection.

FIG. 13. (Color) Time evolution of slopes (a) during pulsed injection and (b) after the cessation of pulsed injection. Different colors indicate different time steps.

pedestal cell. This amount of grains is much smaller than the number of grains in the pedestal cell, because the pedestal is marginally stable at the upper hard limit. Also, beyond a certain critical strength, AGI induces only an increase in ELM frequency without much changes in the amplitude. This is because grains introduced by AGI add to the ejection flux caused by the avalanches.

C. Effect of injection pulse duration in time

In Secs. III A and III B, we have used the simplest form of AGI pulse for the study of the basic ELM mitigation mechanism. However, we can mimic the SMBI experiments more closely by tailoring the AGI pulse shape in the CA model. The pulse duration τ_{dep} is adjusted to match the experimental parameters for SMBI, i.e.,

$$\tau_{dep}/\tau_{ELM} \sim \tau_{dep}^{exp}/\tau_{ELM}^{exp}.$$

Here, the symbols with superscript "*exp*" represent quantities from the experiments.[10]

In Fig. 12, we present the time histories of grain flux induced by the ELM events in the CA, which yields similar information to the H_α signals from experiments. The case without AGI (see Fig. 12(a)) shows unmitigated large fluxes with size $\sim$2000 grains. When we apply AGI with pulse duration $\tau_{dep} = 3\tau_{ELM}$—indicated by the thick black line in Fig. 12(b)—we see the decrease of grain flux $A/A_0 \sim 1/3$ as well as the increase of the frequency $f/f_0 \sim 5$. This result shows qualitative agreement with the experiment, as summarized in Table II.[10] A specially constructed SMBI pulse induces irregular small amplitude transport events, so the

dynamics are incoherent. Although ELM mitigation by SMBI shares the basic physics mechanism with pellet pacing—namely an increase of frequency with a decrease of amplitude—*the observed incoherency is fundamentally different from pellet pacing.* In pacing, small pellet injection is coherently synchronized with the triggered ELMs. For SMBI, injection is not directly correlated with individual ELM events.

It is interesting to observe that there is a time delay for the onset of mitigation. Also, we observe that there is an influence time for AGI effects, i.e., the persistence of the mitigation effect is longer than the AGI pulse duration. In Fig. 12(b), the influence time is roughly $\tau_I \sim 5.1\tau_{ELM}$, which is $8.5 \times 10^{-2}\tau_{pped}$, where τ_{pped} is a pedestal confinement time. After SMBI influence decays, large grain fluxes caused by the global avalanches appear again. The influence time can be viewed as the recovery time for the deformed pedestal to return to its original state. We require deformation of the pedestal gradients for fragmentation of large avalanches. For AGI with a shaped pulse, the change in pedestal gradients requires some time to reach a certain critical level, as shown in Fig. 13(a). The slope 20 steps after AGI initiation does not saturate, as compared to the fully deformed slope. See the slope at 200 steps or 300 steps after AGI initiation shown in Fig. 13(a) (total AGI pulse duration is 600 steps which is $3\tau_{ELM}$). In this sense, the delay time can be understood as the time required to change the pedestal slope by AGI. The persistence time (i.e., after the cessation of pulsed AGI) can be understood as the recovery time from the deformed pedestal gradient to the normal H-mode gradient. In Fig. 13(b), the recovery time (i.e., time for the profile to evolve from the deformed to the usual gradient) is 1000 steps, which is 400

TABLE II. Comparison between experimental and model results.

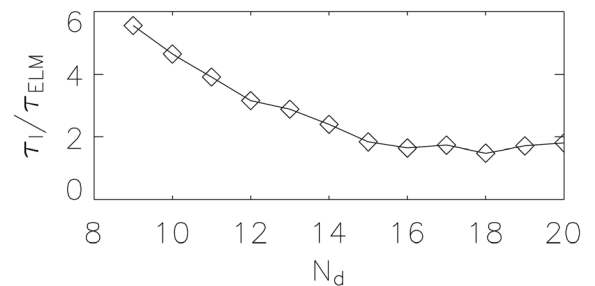|	Experiment	Model
f/f_0	$2 \sim 3.5$	5
A/A_0	1/3	1/3
τ_I	$\sim 3\tau_{ELM}$	$5.1\tau_{ELM}$

FIG. 14. Influence time trend with varying baseline deposition rate. Influence time is normalized by ELM period for the $N_d = 10$ case.
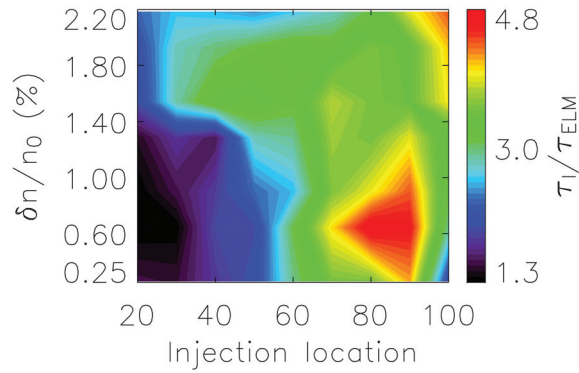
FIG. 15. (Color) Averaged influence time for varying injection location and strength of shaped AGI.

FIG. 17. Edge flux for repetitive pulse injection. The black thick lines indicate times for AGI pulse injection.

steps after the cessation of AGI. Thus, the total influence time persists after active deformation by pulsed AGI, until the full recovery of the gradient.

We test the influence time while varying the baseline deposition rate N_d, as shown in Fig. 14. The injection location is 80, and we use $\delta n/n_0 = 0.6\%$ of AGI which is best for ELM mitigation. Increasing N_d continuously reduces the influence time, until it saturates at $2\tau_{ELM}$. Considering the delay time, the saturated influence time is less than the AGI pulse duration. Thus, a higher baseline deposition rate reduces the recovery time to the unperturbed value.

We performed scans of the influence time for different injection locations and strengths. The influence time is defined as the quiescent time interval before the re-appearance of events with grain flux higher than 1000 (note that the size of flux by an unmitigated "ELM" is around 2000 grains). Figure 15 shows that a long influence time appears for $i = 70 \sim 90$ and $\delta n/n_0 = 0.25 \sim 1.0\%$. We note that this corresponds to the region for effective mitigation
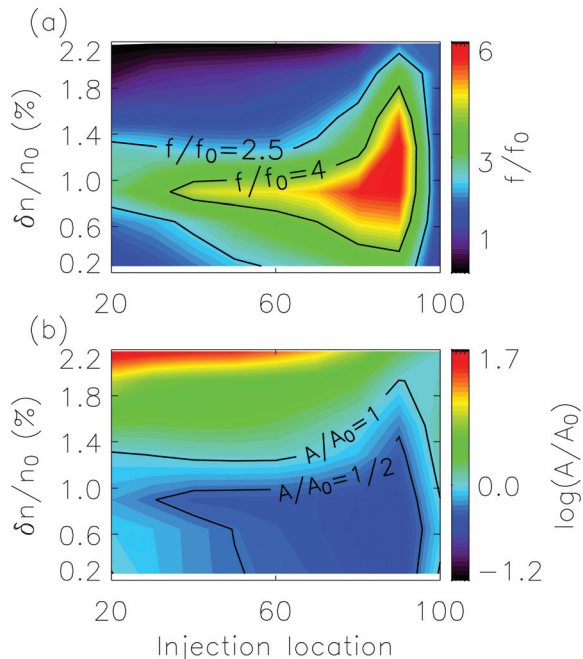

FIG. 16. (Color) Averaged (a) amplitude and (b) frequency for repetitive injection case plotted versus injection location.
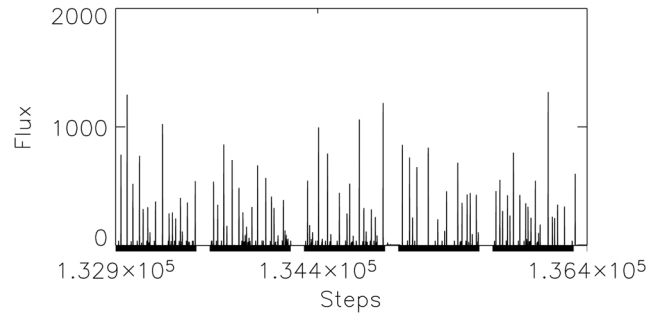
shown as in Fig. 16. This is straightforward to understand if we consider that effective mitigation requires strong deformation of the pedestal profile, which again implies a longer time for recovery to the unperturbed state and so a longer influence time.

Given the discussion of the influence time for mitigation, it is natural to anticipate sustained ELM mitigation by applying AGI with a repetition time shorter than the influence time. This is demonstrated in Fig. 17. Here, we apply AGI with $\tau_{rep} = 0.5\tau_{ELM}$, which is much shorter than the influence time, and observe a sustained state of ELM mitigation. We performed a scan of injection location and strength for shaped AGI's shown as in Fig. 16. For fixed pulse shape, $\tau_{dep} = 3\tau_{ELM}$, the injection location and strength were varied for $i = 20 \sim 100$ and $\delta n/n_0 = 0.2 \sim 2.2\%$, respectively. We can see that injection at the pedestal base is also more effective in the case of repetitive AGI. There appears a critical AGI strength (i.e., $\delta n/n_0$) above which the mitigation effect becomes weaker. Above this effective strength limit, an increase of AGI strength induces an increase in avalanche size. Frequent small size avalanches are replaced by infrequent bigger avalanches. Thus, above the critical level the ELM frequency decreases and mitigation becomes less effective.

IV. DISCUSSION AND CONCLUSION

Since understanding and optimizing ELM mitigation are critical to ITER and since the complexity of the physics involved is beyond the capability of present day "first principles" simulation, a simplified model of ELM dynamics has been constructed. We constructed a bi-stable CA model to study ELM mitigation by SMBI. The effects of SMBI injection were modeled as AGI into the CA system. The key observations using a simple injection model can be summarized as follows:

(i)   It was shown that relatively shallow AGI with sufficient strength can mitigate "ELMs" by replacing the quasi-periodic global avalanches with smaller and more frequent events, i.e., with an increase and decrease of the ELM frequency and amplitude, respectively.

(ii)   The key mechanism of mitigation was the controlled release of the pedestal pressure, i.e., the decrease of the local profile gradient. The resulting inhomogeneities in the pedestal gradients hindered the formation of global discharge events.

(iii)   The scan of injection location and strength showed that the most efficient mitigation is achieved for shallow deposition with sufficient strength. It is necessary to exceed a minimal injection strength to make the gradient of a pedestal cell to exceed the hard gradient limit.

The shaped pulse injection model has shown the following results that are semi-quantitatively consistent with experimental results.

(i)   Shaped pulse injection, adjusted for HL-2 A experiments, exhibits mitigation trends similar to those in the experiment.

(ii)   The influence time is set by the duration of pressure gradient inhomogeneities in the pedestal.

(iii)   Sustained ELM mitigation is possible using SMBI with a repetition rate shorter than influence time.

(iv)   The optimally efficient injection location corresponds to quite shallow deposition.

These features of the mitigation mechanism have merits for application to real tokamaks. We see that deep neutral particle injection, as far pellet injection, is not necessary. Shallow injection of modest amounts of neutral particles is sufficient to mitigate ELMs. SMBI does not require deep penetration of the pedestal.

We propose an ELM mitigation scenario using SMBI, based on aspects of the mitigation processes deduced using the CA model. First, neutrals are deposited by SMBI and ionized in the pedestal. Second, the ionization induces steepening of the local pressure gradient, so the local pressure gradient hits the threshold of ballooning instability. Third, a small ELM is excited and pumps out energy and particles from a narrow regime of the pedestal. Release of energy and particles generates a local pressure gradient inhomogeneity in the pedestal. Fourth, the evolution of large ELMs is disturbed by the local gradient inhomogeneity induced by SMBI and small ELMs. Large ELMs are fragmented. This ELM mitigation scenario may not apply to excitation of small peeling or peeling-ballooning by SMBI, because we don't consider directly the bootstrap current in this simple CA model.

For clarification of the proposed mechanism, we suggest three key experiments. The first one is imaging of the ELM evolution in space and time during SMBI. The predicted fragmentation of ELM at the inhomogeneous pedestal gradient is a key signature of ELM mitigation by SMBI. A fast two dimensional imaging system, like the electron cyclotron emission imaging (ECEI), might be able to observe the evolution of the ELM. The study of 2D ECEI of ELM events in the KSTAR tokamak has already succeeded in observing the growth of ELM filaments.[30] By linking ELM evolution in the pedestal with an inhomogeneity in the pressure gradient, we can validate the fragmentation process predicted by the CA model results.

The second key experiment is the measurement of the pedestal pressure profile during ELM mitigation by SMBI. Gradient inhomogeneity in the pedestal is the key to mitigation, and the length scale of pedestal is a few *cm*. Therefore, we require measurement results having fine scale resolution of less than 1 cm. The measurements need to have a time scale of $\sim$1 ms. In experiments, SMBI pulse duration is of order of a few *ms* and the influence time is shorter than a few tens of *ms*. Thus to measure deformation of the pedestal during mitigation, we need measurements of $\sim$1 ms time scale resolution. Such fine and short time scale measurement by Thomson scattering was conducted on the MAST tokamak[31] and likely is very relevant.

The last key experiment is a direct measurement of the evolution of the frequency spectrum of the particle flux $\langle \tilde{v}_r \tilde{n} \rangle_\omega$. From the results in this paper, we expect that the spectral structure of the transport flux will change during SMBI. In the case without SMBI, the dominant spectral content of $\langle \tilde{v}_r \tilde{n} \rangle_\omega$ is at low frequency, due to large avalanches. In the case of with SMBI, low frequency events are replaced by more frequent high frequency small transport events. Thus, the high frequency spectral content will be stronger than for the case without SMBI. Some experimental results from HL-2 A already have observed this trend, with consistent with our prediction.[10]

We emphasize that these mechanisms rely only on the generic response of the pedestal to external perturbations and not on the exact details of the gradient limit or microturbulence. The trigger of instabilities by steeper pressure profiles and stabilization by weakened profile gradients are generic to all types of MHD instability. Also, we note that recent experiments on HL-2 A and KSTAR hinted that SMBI can mitigate different types of ELMs. Considering the marginal heating powers close to the L-H transition threshold, the ELM in HL-2 A seems to resemble the Type-III variety. On the other hand, the experimental trends in KSTAR seems to indicate those ELMs are more likely to be Type-I. Results from KSTAR suggest that SMBI can effectively mitigate such Type-I ELMs.[32]

Of particular importance is the study of the effect of spatio-temporally rapid changes in pedestal profiles (induced by SMBI) on the peeling-ballooning mode eigenfunction. This offers promise as an explanation of why SMBI appears to successfully mitigate Type-I ELMs. Another important topic is a possible combined synergetic approach using both SMBI and RMP mitigation methods. More sophisticated models for plasma response and SMBI are needed for quantitative studies and comparison with experimental measurements. An extended model including other quantities, e.g., plasma temperature and current profile will give more physical insight into the nature of how various MHD instabilities respond to SMBI injection and the resulting transport and pedestal structure. This will be a subject of our future work.

ACKNOWLEDGMENTS

[1]F. Wagner, Plasma Phys. Controlled Fusion **49**, B1, (2007).

[2]E. J. Doyle, W. A. Houlberg, Y. Kamada, V. Mukhovatov, T. H. Osborne, A. Polevoi, G. Bateman, J. W. Connor, J. G. Cordey, T. Fujita, X. Garbet, T. S. Hahm, L. D. Horton, A. E. Hubbard, F. Imbeaux, F. Jenko, J. E. Kinsey, Y. Kishimoto, J. Li, T. C. Luce, Y. Martin, M. Ossipenko, V. Parail, A. Peeters, T. L. Rhodes, J. E. Rice, C. M. Roach, V. Rozhansky, F. Ryter, G. Saibene, R. Sartori, A. C. C. Sips, J. A. Snipes, M. Sugihara, E. J. Synakowski, H. Takenaga, T. Takizuka, K. Thomsen, M. R. Wade, H. R. Wilson, ITPA Transport Physics Topical Group, ITPA Confinement Database and Modelling Topical Group, and ITPA Pedestal and Edge Topical Group, Nucl. Fusion **47**, S18 (2007).

[3]P. T. Lang, J. Neuhauser, L. D. Horton, T. Eich, L. Fattorini1, J. C. Fuchs, O. Gehre, A. Herrmann, P. Ignácz, M. Jakobi, S. Kálvin, M. Kaufmann, G. Kocsis, B. Kurzan, C. Maggi, M. E. Manso, M. Maraschek, V. Mertens, A. Mück, H. D. Murmann, R. Neu, I. Nunes, D. Reich, M. Reich, S. Saarelma, W. Sandmann, J. Stober, U. Vogl, and the ASDEX Upgrade Team, Nucl. Fusion **43**, 1110 (2003).

[4]P. T. Lang, G. D. Conway, T. Eich, L. Fattorini, O. Gruber, S. Günter, L. D. Horton, S. Kalvin, A. Kallenbach, M. Kaufmann, G. Kocsis, A. Lorenz, M. E. Manso, M. Maraschek, V. Mertens, J. Neuhauser, I. Nunes, W. Schneider, W. Suttrop, H. Urano, and the ASDEX Upgrade Team, Nucl. Fusion **51**, 665 (2004).

[5]L. R. Baylor, T. C. Jernigan, P. B. Parks, G. Antar, N. H. Brooks, S. K. Combs, D. T. Fehling, C. R. Foust, W. A. Houlberg, and G. L. Schmidt, Nucl. Fusion **47**, 1598 (2007).

[6]T. C. Hender, R. Fitzpatrick, A. W. Morris, P. G. Carolan, R. D. Durst, T. Edlington, J. Ferreira, S. J. Fielding, P. S. Haynes, J. Hugill, I. J. Jenkins, R. J. La Haye, B. J. Parham, D. C. Robinson, T. N. Todd, M. Valovic, and G. Vayakis, Nucl. Fusion **32**, 2091 (1992).

[7]T. E. Evans, R. A. Moyer, P. R. Thomas, J. G. Watkins, T. H. Osborne, J. A. Boedo, E. J. Doyle, M. E. Fenstermacher, K. H. Finken, R. J. Groebner, M. Groth, J. H. Harris, R. J. La Haye, C. J. Lasnier, S. Masuzaki, N. Ohyabu, D. G. Pretty, T. L. Rhodes, H. Reimerdes, D. L. Rudakov, M. J. Schaffer, G. Wang, and L. Zeng, Phys. Rev. Lett. **92**, 235003 (2004).

[8]T. E. Evans, R. A. Moyer, K. H. Burrell, M. E. Fenstermacher, I. Joseph, A. W. Leonard, T. H. Osborne, G. D. Porter, M. J. Schaffer, P. B. Snyder, P. R. Thomas, J. G. Watkins, and W. P. West, Nat. Phys. **2**, 419 (2006).

[9]L. Yao, B. Feng, C. Chen, Z. Shi, B. Yuan, Y. Zhou, X. Duan, H. Sun, J. Lu, Y. Jiao, G. Ni, H. Lu, W. Xiao, W. Li, Y. Pan, W. Hong, H. Ran, X. Ding, and Y. Liu, Nucl. Fusion **47**, 1399 (2007).

[10]W. W. Xiao, P. H. Diamond, X. L. Zou, J. Q. Dong, X. T. Ding, L. H. Yao, B. B. Feng, C. Y. Chen, W. L. Zhong, M. Xu, B. S. Yuan, T. Rhee, J. M. Kwon, Z. B. Shi, J. Rao, G. J. Lei, J. Y. Cao, J. Zhou, M. Huang, D. L. Yu, Y. Huang, K. J. Zhao, Z. Y. Cui, X. M. Song, Y. D. Gao, Y. P. Zhang, J. Cheng, X. Y. Han, Y. Zhou, Y. B. Dong, X. Q. Ji, Q. W. Yang, Yi Liu, L. W. Yan, X. R. Duan, Yong Liu, and HL-2A team, "ELM mitigation by supersonic molecular beam injection into the H-mode pedestal in HL-2A tokamak," Nucl. Fusion (submitted).

[11]J. Kim, Y-.M. Jeon, W. W. Xiao, S-.W. Yoon, J-.K. Park, G. S. Yun, J. Ahn, H. S. Kim, H-.L. Yang, H. K. Kim, S. Park, J. H. Jeong, M. Jung, G. H. Choe, W. H. Ko, S-.G. Lee, Y. U. Nam, J. G. Bak, K. D. Lee, H. K. Na, S-.H. Hahn, P. H. Diamond, T. Rhee, J. M. Kwon, S. A. Sabbagh, Y. S. Park, H. K. Park, Y. S. Na, W. C. Kim, J. G. Kwak, and the KSTAR contributors, "ELM control experiments in the KSTAR Device," Nucl. Fusion (submitted).

[12]I. Gruzinov, P. H. Diamond, and M. N. Rosenbluth, Phys. Rev. Lett. **89**, 25 (2002).

[13]B. A. Carreras, V. E. Lynch, P. H. Diamond, and M. Medvedev, Phys. Plasmas **5**, 1206 (1998).

[14]S. C. Chapman, Phys. Rev. E **62**, 1905 (2000).

[15]D. E. Newman, B. A. Carreras, P. H. Diamond, and T. S. Hahm, Phys. Plasmas **3**, 1858 (1996).

[16]D. E. Newman, B. A. Carreras, and P. H. Diamond, Phys. Lett. A **218**, 58 (1996).

[17]R. Sánchez, D. E. Newman, and B. A. Carreras, Nucl. Fusion **41**, 247 (2001).

[18]F. Sattin and M. Baiesi, Phys. Rev. Lett. **96**, 105005 (2006).

[19]S. C. Chapman, R. O. Dendy, and B. Hnat, Plasma Phys. Controlled Fusion **45**, 301 (2003).

[20]R. Sánchez, D. E. Newman, B. A. Carreras, R. Woodard, W. Ferenbaugh, and H. R. Hicks, Nucl. Fusion **43**, 1031 (2003).

[21]I. Gruzinov, P. H. Diamond, and M. N. Rosenbluth, Phys. Plasmas **10**, 569 (2003).

[22]ITER Physics Expert Groups on Confinement and Transport and Confinement Modelling and Database, ITER Physics Basis Editors, and ITER-EDA, Nucl. Fusion **39**, 2175 (1999).

[23]P. H. Diamond and T. S. Hahm, Phys. Plasmas **2**, 3640 (1995).

[24]H. L. Hinton, Phys. Fluids B, **3** 696 (1991).

[25]H. Wilson, Fusion Sci. Technol. **53**, 161 (2008).

[26]C. E. Kessel, Nucl. Fusion **34**, 1221 (1994).

[27]D. E. Newman, R. Sánchez, B. A. Carreras, and W. Ferenbaugh, Phys. Rev. Lett. **88**, 204304 (2002).

[28]J. A. Boedo, D. L. Rudakov, R. A. Moyer, G. R. McKee, R. J. Colchin, M. J. Schaffer, P. G. Stangeby, W. P. West, S. L. Allen, T. E. Evans, R. J. Fonck, E. M. Hollmann, S. Krasheninnikov, A. W. Leonard, W. Nevins, M. A. Mahdavi, G. D. Porter, G. R. Tynan, D. G. Whyte, and X. Xu, Phys. Plasmas **10**, 1670 (2003).

[29]T. Hwa and M. Kardar, Phys. Rev. A **45**, 7002 (1992).

[30]G. S. Yun, W. Lee, M. J. Choi, J. Lee, H. K. Park, B. Tobias, C. W. Domier, N. C. Luhmann, Jr., A. J. H. Donne, J. H. Lee, and KSTAR Team, Phys. Rev. Lett. **107**, 045004 (2011).

[31]K. J. Gibson, N. Barratt, I. Chapman, N. Conway, M. R. Dunstan, A. R. Field, L. Garzotti, A. Kirk, B. Lloyd, H. Meyer, G. Naylor, T. O. Gorman, R. Scannell, S. Shibaev, J. Snape, G. J. Tallents, D. Temple, A. Thornton, S. Pinches, M. Valovic, M. J. Walsh, H. R. Wilson, and the MAST team, Plasma Phys. Controlled Fusion **52**, 124041 (2010).

[32]W. W. Xiao, P. H. Diamond, W. C. Kim, S. W. Yoon, J. Kim, S. H. Hahn, G. S. Yun, J. G. Bak, Y. U. Nam, J. W. Ahn, H. K. Kim, H. T. Kim, K. P. Kim, H. K. Park, G. H. Choe, M. J. Choi, J. I. Song, S. G. Lee, T. Rhee, J. M. Kwon, Y. J. Shi, K. D. Lee, W. H. Ko, Y. W. Yu, S. I. Park, M. Jung, Y. S. Bae, J. G. Kwak, M. Kwon, and KSTAR team, "First signature of type-I ELM mitigation by supersonic molecular beam injection in KSTAR," Phys. Rev. Lett. (submitted).